

**On the Verwey transition in magnetite:
the soft modes of the metal-insulator transition**

S. Borroni^{†,1} E. Baldini^{†,1,2} A. Mann,¹ C. Arrell,² F. van Mourik,² J. Teyssier,³ J. Lorenzana,⁴ and F. Carbone*¹

¹*Laboratory for Ultrafast Microscopy and Electron Scattering,
ICMP, École Polytechnique Fédérale de Lausanne,
CH-1015 Lausanne, Switzerland*

²*Laboratory for Ultrafast Spectroscopy,
ISIC, École Polytechnique Fédérale de Lausanne,
CH-1015 Lausanne, Switzerland*

³*Department of Quantum Matter Physics,
University of Geneva,
CH-1211 Geneva, Switzerland*

⁴*Institute for Complex Systems - CNR, and Physics Department,
University of Rome "La Sapienza",
I-00185 Rome, Italy*

(Dated: May 11, 2022)

[†] These authors contributed equally to this work.

*Corresponding author: fabrizio.carbone@epfl.ch.

Abstract

Fe_3O_4 is the earliest discovered magnetic material. It is widely used in recording devices or as a catalyst [1, 2], and some of its electronic and magnetic properties hold promise for future applications [3]. Magnetite undergoes a structural phase transition (PT) accompanied by a Metal-Insulator Transition (MIT) below 120 K, which was originally proposed by Verwey to be driven by the onset of a periodic modulation of the charge on the iron sites [4]. While the pattern of the charge ordering has been shown to be far more complex than the original Verwey hypothesis [5, 6], the mechanism behind its formation is still a subject of debate. As an alternative to a purely electronic model, the interplay between structural and electronic degrees of freedom has been proposed to drive the MIT [7, 8]. However, direct evidence for the involvement of the structure has never been obtained, since no clear anomalies of any phonon mode have been observed across the critical region. Here, we reveal by means of ultrafast broadband optical spectroscopy and spontaneous Raman scattering that the primary order parameters of the structural PT are strongly coupled to the charge density wave, and undergo a sizable softening in the proximity of the critical temperature. Furthermore, we show that signatures of the low-temperature phase can be induced by impulsive charge transfer excitation even at room temperature, where fluctuations of the charge order have recently been shown to persist [9]. These results clarify the mechanism for the Verwey transition and open novel scenarios in the coherent control of MITs.

At room temperature, the ground state of magnetite is metallic ferrimagnetic and the crystalline structure is an inverse cubic spinel, in which tetrahedrally coordinated Fe A-sites are occupied only by Fe^{3+} ions, while octahedrally coordinated Fe B-sites are occupied by an equal number of Fe^{3+} and Fe^{2+} ions. Below the Verwey temperature T_V ($= 116$ K in our sample), magnetite lowers its crystal symmetry to monoclinic and a two orders of magnitude decrease of the dc conductivity is observed [10]. The insulating behaviour is the result of the long-range charge and orbital ordering that emerges among the B-sites when crossing the PT.

In the original Verwey hypothesis [4], below T_V the $a/4$ -spaced $[001]_c$ lattice planes (where a is the lattice parameter) are alternatively occupied by Fe^{2+} and Fe^{3+} ions, whereas above T_V the latter cations are randomly distributed, allowing the electron transport in the conductive phase. Although this scenario proves correct to a first approximation, recently a more complex electronic order was identified below T_V [6]. Signatures of such a charge ordering have been found to persist in the form of short-range correlations all the way to room temperature [9].

Details about the atomic distortions involved in the Verwey transition have been obtained via optical spectroscopy [11], Raman spectroscopy [12, 13], X-ray diffraction [5, 6, 14, 15] and elastic as well as inelastic neutron scattering [5, 16, 17]. In particular, a subset of phonons belonging to the Δ and X class become static distortions below the Verwey transition, yielding the monoclinic unit cell [7, 8, 15, 16]. An alternative scenario to the original Verwey hypothesis was put forth by Yamada, which stated that the condensation of a fluctuating charge order coupled to a Δ_5 lattice distortion would drive the MIT [18]. Recently, it was theoretically proposed that both the Δ_5 and X_3 modes are the primary order parameters of the structural PT and their strong coupling to the conduction band electrons is responsible for the opening of the gap at the Fermi surface across the MIT [7]. However, the question whether a combined structural-electronic mechanism is responsible for the MIT in magnetite is still open because anomalies of the structural modes at the critical temperature are expected in these scenarios, but so far have not been observed [19].

A natural single crystal of magnetite was cut and polished along the $[110]_c$ plane. Its characterization is reported in the Supplementary Information (SI). Ultrafast optical spectroscopy was carried out in the temperature range between 5 and 300 K. Briefly, a laser pulse tuned to the O $2p$ - Fe $3d$ charge transfer excitation (3.1 eV) [11] (see SI) and shorter

than the vibrational period of the phonon modes of the crystal (45 fs) induces coherent vibrations of the ions. Such vibrations modulate the optical properties of the sample, which are monitored by reflecting a weaker white light (1.75-2.9 eV) pulse from its surface. The time-delay between the two pulses is varied to obtain a sequence of time points representative of the photo-induced dynamics of the material. This mechanism is described in the framework of the Impulsive Stimulated Raman Scattering (ISRS) mechanism [20] (see SI). The spontaneous Raman response of the material is also monitored in the same temperature range. The details of the experimental setups are described in the Methods section.

Fig. 1a, b and c show the transient reflectivity ($\Delta R/R$) spectra as a function of pump-probe time-delay at an absorbed fluence of 3 mJ/cm² and temperatures of 10, 120 and 300 K, respectively (the full set of data of the temperature dependence is included in Fig. S4 of the SI). The temporal traces obtained from an average between 1.85 and 2.15 eV probe photon energy are displayed as a function of temperature in Fig. 1d. In Fig. 1e, the residuals from a multi-exponential fit to the temporal traces are shown, revealing coherent oscillations above and below T_V , with periods between 100 and 500 fs.

To assign these modes, a direct comparison between the phonon dispersions and our time-resolved experiments is carried out. In Fig. 2b, the theoretical and experimental dispersions of the phonon modes of magnetite in the cubic high-temperature phase are represented by blue lines [7, 8, 17]. In the low-temperature phase, the structural PT causes a quadrupling of the unit cell, resulting in new phonon branches which are shown by red traces in Fig. 2b. As a result, various structural modes can be found at the Γ point of the Brillouin Zone (BZ) below the structural PT (highlighted as full symbols on the energy axis and labelled according to previous reports [8, 17]), thus being potentially observable by visible-light Raman scattering (RS). In Fig. 2a, the ISRS spectrum at 120 K is displayed. Here, five distinct regions are identified: i) the Δ_5 region below 9 meV, ii) the X_4 region between 9 and 15 meV, iii) the X_3 region between 15 and 22 meV, iv) the t_{2g} region between 22 and 26 meV and v) the X_1 region between 26 and 35 meV. Peaks around 13 and 20 meV were also found in independent spontaneous Raman experiments on thin films at low temperature [13]. In our own spontaneous Raman experiments, peaks around 20 and 15 meV were observed to develop below T_V and assigned to the X_3 and X_4 modes, respectively. Instead, the Δ_5 region was not accessible to our Raman spectrometer. The whole spontaneous Raman spectrum and its temperature dependence are discussed in detail in the SI.

The temperature dependence of the normalized Fourier transform (FT) of the residuals from a multi-exponential fit to the transient reflectivity data is displayed in Fig. 3a and b. Both the strongest oscillations observed, assigned to the Δ_5 and X_3 modes, are found to red-shift as the temperature approaches T_V . Remarkably, while their intensity is strongly suppressed in the metallic phase, they are still visible all the way to room temperature, opening the possibility to study the effect of their coupling with the charge density wave (CDW). Their energy is plotted as a function of temperature in Fig. 3d and e, together with the maximum $|\Delta R/R|$ signal observed at a probe photon energy of 2.1 eV. As in Ref. [3], a marked increase in the $|\Delta R/R|$ response characterizes the onset of the insulating phase; our data suggest that the softening of the modes is maximum at a temperature somewhat higher than the MIT.

In spontaneous RS experiments, only the temperature dependence of the X_3 mode could be followed up to T_V , while any possible response in the high-temperature phase is below the background noise (see Fig. 3c).

To explore the mechanism responsible for the coherent excitation of the CDW related modes above T_V , we perform a fluence dependence at 120 K (slightly above T_V in our sample). In Fig. 4a and b, the FT of the oscillations obtained at an absorbed fluence of 3, 17 and 27 mJ/cm² are shown. The coherent oscillations are enhanced by stronger light excitation, all the way to the damage threshold of the material, which is found to occur at an absorbed fluence of 33 mJ/cm².

In the high-temperature phase, however, the Δ_5 and X_3 phonon modes are not found at the Γ point of the BZ and should not be accessible via either impulsive or spontaneous RS experiments (see Fig. 2b). We argue that these modes become Raman active with the assistance of CDW fluctuations which have been shown to persist above T_V [9, 21]. The CDW fluctuations provide the $(00\frac{1}{2})$ and (001) wave-vector components (in units of $2\pi/a$) [5] required to satisfy the momentum conservation rule in a Raman process, involving the emission of a phonon plus a CDW mode. Such a process is pictorially represented in Fig. 4d and discussed in detail in the SI.

Fig. 4c displays the strength of the X_3 modes as a function of the absorbed fluence at 120 K. Below 3 mJ/cm², the spectral weight of the X_3 modes is comparable to the background level of our experiments. Such a fluence dependence is clearly non-linear and shows a sharp increase of the oscillation strength upon more intense photo-excitation. We attribute this

effect to a laser-induced stabilization of the low-temperature CDW phase by the same Raman coupling which allows the observation of the modes above T_V (see SI). Moreover, the fluence dependence suggests that the visibility of the modes above T_V is an effect of the stronger excitation in ISRS compared to spontaneous RS combined with a better sensitivity.

The observation of the softening behavior of the Δ_5 and X_3 modes confirms that the MIT in magnetite is a structural/charge interrelated process, contradicting the original Verwey hypothesis for which it should have been a purely electronic effect. Moreover, it highlights the importance of the Δ_5 symmetry, which was not present in the original hypothesis either. Complete softening of the modes is only expected in a second order phase transition. In magnetite, the MIT is known to be of first-order character [4], which naturally explains our observation of a partial softening of the modes coupled to the CDW.

The possibility to observe the Δ_5 and X_3 modes above T_V allows us to speculate about the nature of the photo-induced metallic phase. Recent experiments have suggested that the metallic phase can be photo-excited within 1-2 ps in magnetite [3]. We refine this scenario by pointing out that, while Bragg reflections of the CDW phase are suppressed by strong laser pulses, dynamic correlations having Δ_5 and X_3 symmetries are reinforced and likely dress carriers above the PT. Our experiments are sensitive to this mechanism because by photo-exciting the Fe-O charge transfer, sudden changes of the d -orbital occupancy are caused, to which the charge order is very sensitive.

Typically, ultrashort laser pulses are used to melt the low-temperature order parameter and establish the high-temperature phase properties, for example, triggering an insulator-to-metal transition [3]. Instead, in our experiments, tailored optical pulses are used to transiently promote the ordered state while the solid is kept above the ordering temperature, providing a novel perspective in the control of transition metal oxides by light.

METHODS

Ultrafast broadband optical spectroscopy

A 2 mm thick single crystal of natural magnetite, cleaved along the $[110]_c$ plane, was fixed to a copper cold-finger cryostat; the easy axis of the magnetization $[111]_c$ was perpendicular to the incidence plane of the s-polarized laser light. The temperature was varied between 10 and 300 K, in a vacuum of 10^{-8} mbar. The output of an amplified Ti:Sapphire laser delivering 50 fs pulses centred at 1.55 eV at a repetition rate of 6 kHz was split into a pump and a probe beam. The pump beam was used to photo-excite the material at 3.1 eV, after frequency doubling the fundamental in a beta-barium borate crystal, while the probe beam was focused into a CaF_2 crystal to generate broadband pulses from 1.75 to 2.9 eV. The spectra were recorded by a fiber-coupled spectrometer. A chopper modulated the train of pump pulses at a frequency of 3 kHz, so that at every delay time a difference between the pumped and unpumped spectrum was taken, yielding a sensitivity down to 10^{-4} in $\Delta R/R$. Further details of the set-up are given in Refs. [22, 23].

Spontaneous Raman scattering

The sample was mounted on a holder in thermal contact with the copper cold-finger of a closed-cycle helium cryostat and the temperature was scanned between 5 and 300 K in a base pressure of 10^{-6} mbar. Raman spectra were measured as a function of temperature by means of a home-made Raman spectrometer with $\sim 5 \text{ cm}^{-1}$ resolution, using the 2.41 eV emission line of an argon laser, with a $2 \mu\text{m}$ spot size at the sample surface and 7 mW of delivered power. The optical filter used to block Rayleigh scattered light set the lower limit to the detected Raman shift to $\sim 75 \text{ cm}^{-1}$.

ACKNOWLEDGEMENTS

We acknowledge D. Fausti, O. Yazyev, A. B. Kuzmenko and D. McGrouther for useful discussions, M. Prester and D. Drobac (Institute of Physics, Zagreb) for the AC susceptibility characterization, and A. Pisoni (Laboratory of Physics of Complex Matter, École Polytechnique Fédérale de Lausanne, Lausanne) for the resistivity characterization. Work at LUMES was supported by NCCR MUST and by the ERC starting grant USED258697.

-
- [1] Hoagland, A. S. History of magnetic disk storage based on perpendicular magnetic recording. *IEEE Trans. Magn.* **39**, 1871-1875 (2003).
- [2] Hu, A., Yee, G. T. & Lin, W. Magnetically recoverable chiral catalysts immobilized on magnetite nanoparticles for asymmetric hydrogenation of aromatic ketones. *J. Am. Chem. Soc.* **36**, 12486-7 (2005).
- [3] de Jong, S. et al. Speed limit of the insulator-metal transition in magnetite. *Nature Mater.* **12**, 882–886 (2013).
- [4] Verwey, E. J. W. Electronic conduction of magnetite (Fe_3O_4) and its transition point at low temperatures. *Nature* **144**, 327-328 (1939).
- [5] Wright, J. P., Attfield, J. P. & Radaelli, P. G. Long range charge ordering in magnetite below the Verwey transition. *Phys. Rev. Lett.* **87**, 266401 (2001).
- [6] Senn, M. S., Wright, J. P. & Attfield, J. P. Charge order and three-site distortions in the Verwey structure of magnetite. *Nature* **481**, 173-176 (2012).
- [7] Piekarz, P., Parlinski, K. & Oleś, A. M. Mechanism of the Verwey Transition in Magnetite. *Phys. Rev. Lett.* **97**, 156402 (2006).
- [8] Piekarz, P., Parlinski, K. & Oleś, A. M. Origin of the Verwey transition in magnetite: Group theory, electronic structure, and lattice dynamics study. *Phys. Rev. B* **76**, 165124 (2007).
- [9] Bosak, A. et al. Short-range correlations in magnetite above the Verwey temperature. *Phys. Rev. X* **4**, 011040 (2014).
- [10] Imada, M., Fujimori, A. & Tokura, Y. Metal-insulator transitions. *Rev. Mod. Phys.* **70**, 1039-1263 (1998).
- [11] Park, S. K., Ishikawa, T. & Tokura, Y. Charge-gap formation upon the Verwey transition in Fe_3O_4 . *Phys. Rev. B* **58**, 3717-3720 (1998).
- [12] Gasparov, L. V. et al. Infrared and Raman studies of the Verwey transition in magnetite. *Phys. Rev. B* **62**, 7939-7944 (2000).
- [13] Yazdi, M. B., Choi, K. Y., Wulferding, D., Lemmens, P. & Alff, L. Raman study of the Verwey transition in magnetite thin films. *New J. Phys.* **15**, 103032 (2013).
- [14] Yoshida, J. & Iida, S. X-ray diffraction study on the low temperature phase of magnetite. *J. Phys. Soc. Jpn.* **42**, 230-237 (1977).

- [15] Blasco, J., García, J. & Subías, G. Structural transformation in magnetite below the Verwey transition. *Phys. Rev. B* **83**, 104105 (2011).
- [16] Iizumi, M. et al. Structure of magnetite (Fe_3O_4) below the Verwey transition temperature. *Acta Cryst. B* **38**, 2121-2133 (1982).
- [17] Samuelsen, E. J. & Steinsvoll, O. Low-energy phonons in magnetite. *Phys. Stat. Sol. B* **61**, 615-620 (1974).
- [18] Yamada, Y. Charge ordering and lattice instability in magnetite. *20th Conf. on Magn. and Magn. Mater.* **24**, 79-85 (1975).
- [19] Hoesch, M. et al. Anharmonicity due to Electron-Phonon Coupling in Magnetite. *Phys. Rev. Lett.* **110**, 207204 (2013).
- [20] Stevens, T. E., Kuhl, J. & Merlin, R. Coherent phonon generation and the two stimulated Raman tensors. *Phys. Rev. B* **65**, 144304 (2002).
- [21] Fujii, Y., Shirane, G. & Yamada, Y. Study of the 123-K phase transition of magnetite by critical neutron scattering. *Phys. Rev. B* **11**, 2036-2041 (1975).
- [22] Mann, A. et al. Probing the electron-phonon interaction in correlated systems with coherent lattice fluctuation spectroscopy. *Phys. Rev. B* to be published.
- [23] Mansart, B. et al. Coupling of a high-energy excitation to superconducting quasiparticles in a cuprate from coherent charge fluctuation spectroscopy. *Proc. Natl. Acad. Sci.* **110**, 4539-4544 (2013).
- [24] Skumryev, V., Blythe, H. J., Cullen, J. & Coey, J. M. D. AC susceptibility of a magnetite crystal. *J. Magn. Magn. Mater.* **196**, 515-517 (1999).
- [25] Bałanda, M. et al. Magnetic AC susceptibility of stoichiometric and low zinc doped magnetite single crystals. *Eur. Phys. J. B* **43**, 201-212 (2005).
- [26] Maldague, P. F. Optical spectrum of a Hubbard chain. *Phys. Rev. B* **16**, 2437-2446 (1977).
- [27] Zhang, Z. & Satpathy, S. Electron states, magnetism, and the Verwey transition in magnetite. *Phys. Rev. B* **44**, 13319 (1991).
- [28] Leonov, I., Yaresko, A. N., Antonov, V. N. & Anisimov, V. I. Electronic structure of charge-ordered Fe_3O_4 from calculated optical, magneto-optical Kerr effect, and O K -edge x-ray absorption spectra. *Phys. Rev. B* **74**, 165117 (2006).
- [29] Shebanova, O. N. & Lazor, P. Raman study of magnetite (Fe_3O_4): laser-induced thermal effects and oxidation. *J. Raman Spectrosc.* **34**, 845-852 (2003).

- [30] Cardona M. Light Scattering in Solids II: Basic Concepts and Instrumentation. *Springer-Verlag* (1982).
- [31] Merlin R. Generating coherent THz phonons with light pulses. *Solid State Comm.* **102**, 207-220 (1997).
- [32] Lorenzana, J. et al., Investigating pairing interactions with coherent charge fluctuation spectroscopy. *Europ. Phys. J. Spec. Top.* **222**, 1223-1239 (2013).

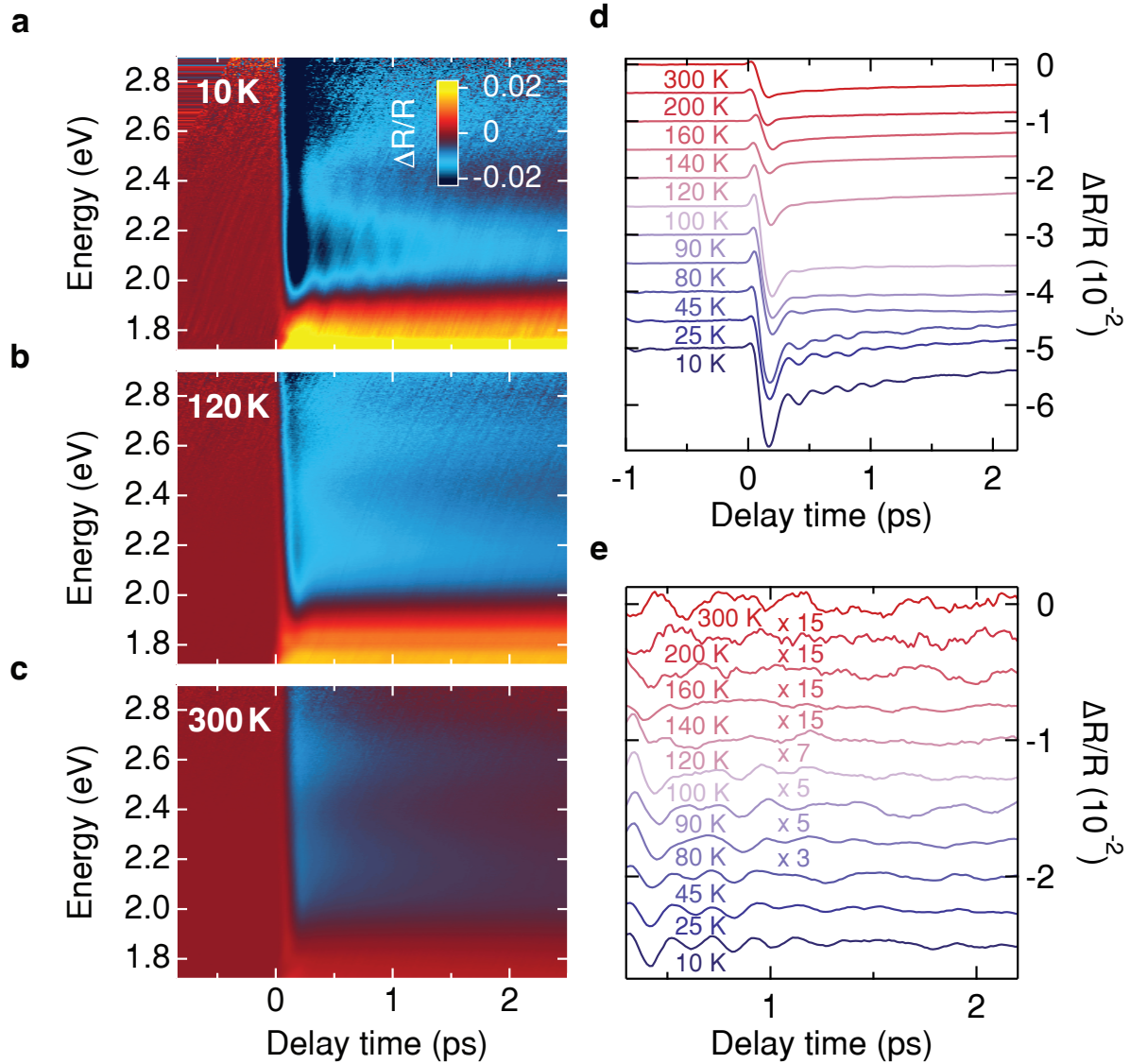


FIG. 1. Ultrafast optical response of magnetite.

a, b, c Colour maps of the transient reflectivity $\Delta R/R$ as a function of probe photon energy and pump-probe delay time at an absorbed fluence of 3 mJ/cm^2 and temperatures of 10, 120 and 300 K, respectively. d Temperature dependence of the $\Delta R/R$ signal as a function of time, averaged between 1.85 and 2.15 eV probe photon energy. e Temperature dependence of the residuals from a multi-exponential fit to the temporal traces in panel d.

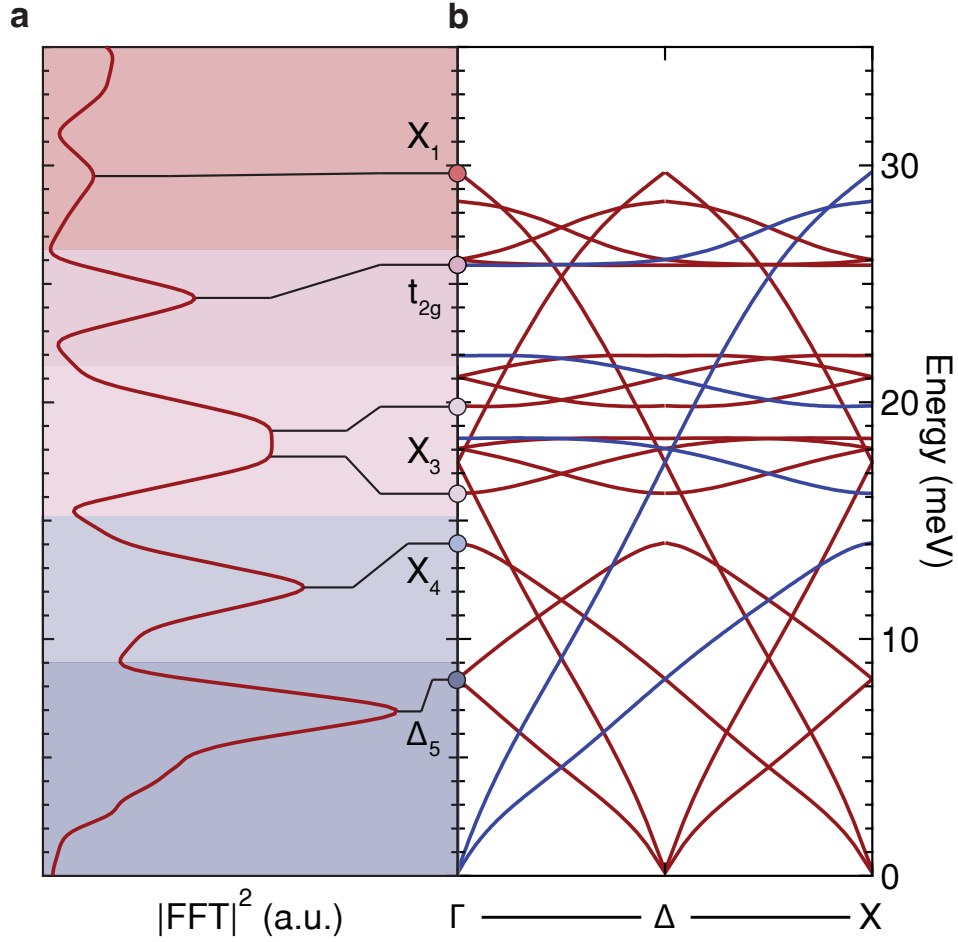


FIG. 2. **Mode assignment.**

a Experimental spectrum obtained at 120 K by ISRS. Different background colors highlight the energy ranges that correspond to the Δ_5 , X_4 , X_3 , t_{2g} and X_1 modes. The same colour legend is used in Fig. 2b to identify the new phonon modes that become active at Γ in the low-temperature phase. **b** Theoretical and experimental dispersion of the phonon modes of magnetite in the cubic high-temperature phase (blue lines) between the Γ and X points of the BZ, obtained from [7, 8, 17]. The red traces identify the new phonon branches resulting from the quadrupling of the unit cell in the low-temperature phase.

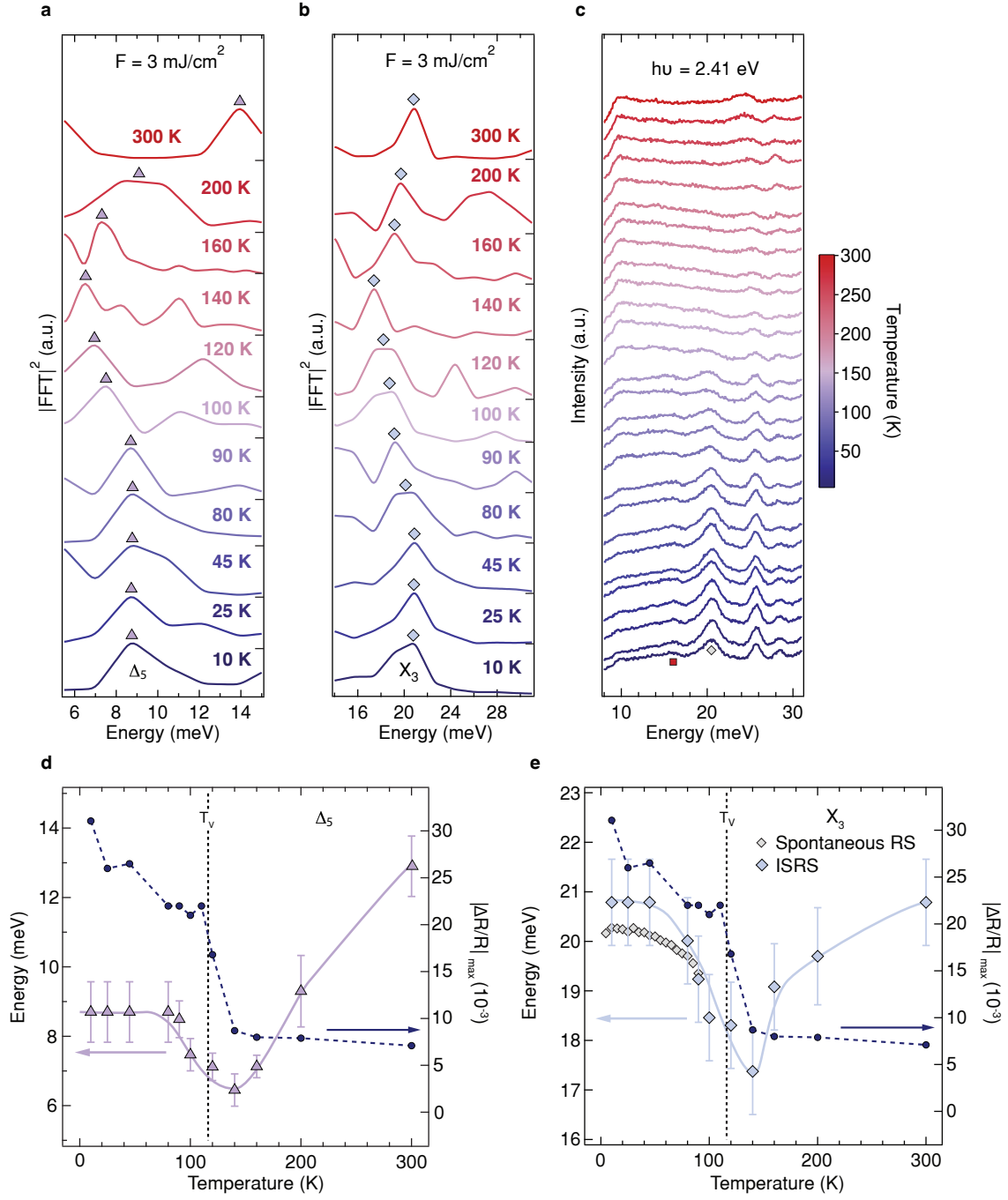


FIG. 3.

FIG. 3. **Phonon softening.**

a-b Fourier transform analysis of the coherent oscillations in the transient reflectivity signal for different temperatures. The Δ_5 and X_3 modes are shown in the normalized FTs as violet triangles and light-blue diamonds, respectively. All the normalized FTs have been obtained from the residuals of a multi-exponential fit to the $\Delta R/R$ maps at an absorbed fluence of 3 mJ/cm^2 , by averaging the signal over the spectral ranges where the Δ_5 and X_3 modes are strongest. **c** Spontaneous RS spectra as a function of temperature from 5 to 300 K. The excitation energy is 2.41 eV. The X_4 and X_3 modes are highlighted with a red square and a grey diamond, respectively. **d-e** Temperature dependence of the energy of the modes from spontaneous RS and ultrafast broadband optical spectroscopy. The Δ_5 and X_3 mode energies obtained from the FT of Fig. 3a-b are respectively indicated by violet triangles and light-blue diamonds, while the X_3 mode energies from spontaneous RS are represented via small grey diamonds. In both figures, blue circles represent the maximum $|\Delta R/R|$ ($\sim 200 \text{ fs}$) at all temperatures, showing the MIT [3]. T_V is highlighted through a dashed vertical line. Lines are guides to the eye.

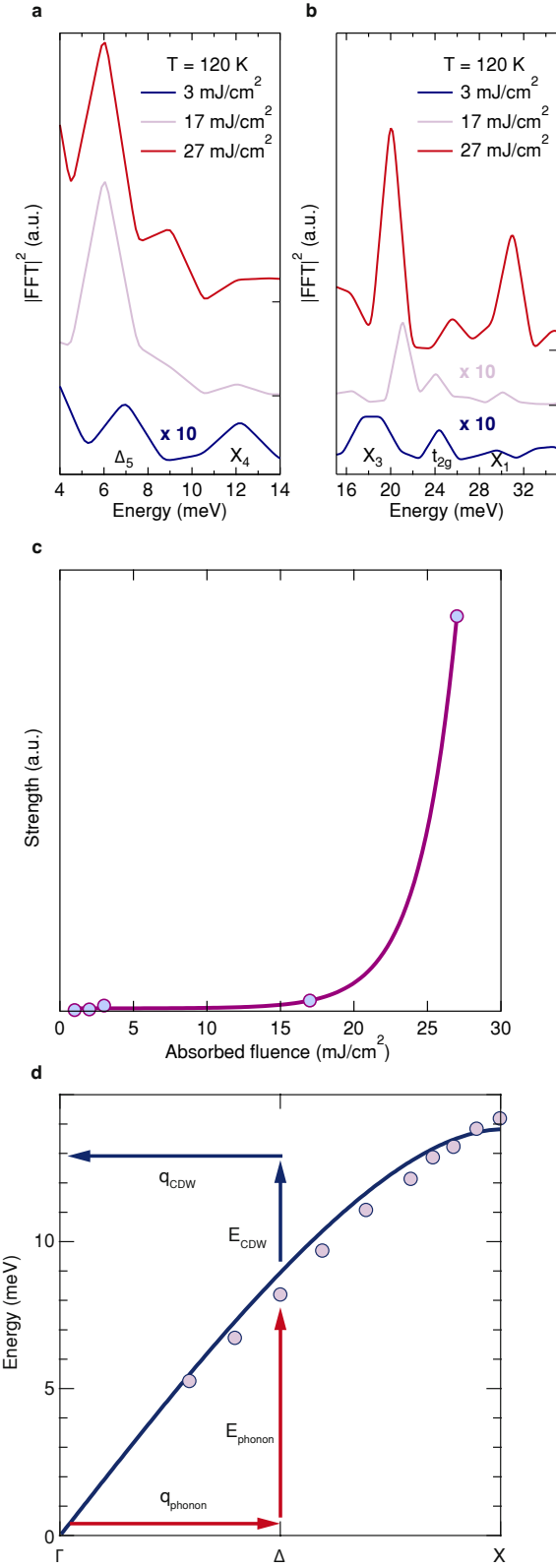


FIG. 4.

FIG. 4. **Fluence dependence at 120 K and photo-excitation mechanism above T_V .**

a-b Fourier transform analysis of the coherent oscillations in the transient reflectivity signal at 120 K for different values of absorbed fluence. The Δ_5 , X_4 , X_3 , t_{2g} and X_1 modes are identified in the FT. All the FTs have been obtained from the residuals of a multi-exponential fit to the $\Delta R/R$ maps, by averaging the signal over the spectral ranges where the Δ_5 and X_3 modes are strongest. **c** Strength of the X_3 modes as a function of fluence at 120 K (light blue circles) calculated as the peak values of the corresponding features in the FTs, with reference to the spectral range where the X_3 modes are strongest. The experimental data are fitted with an exponential function (violet solid line). **d** Schematic representation of energy-momentum conservation rules in the photo-excitation mechanism of the Δ_5 mode and the CDW above T_V . The phonon dispersion as obtained from inelastic neutron scattering (violet circles) and the density functional theory calculations of Ref. [19] (blue solid line) is shown. The energy and momentum of the Δ_5 phonon mode and the CDW mode are represented by red and blue arrows, respectively. The combination of the phonon and the CDW allows the energy-momentum conservation in the optical excitation process.

SUPPLEMENTARY INFORMATION

S1. SAMPLE CHARACTERIZATION

In our experiments, a 2 mm thick single crystal of natural magnetite cleaved along the $[110]_c$ plane was used. The sample resistivity and AC magnetic susceptibility were measured as a function of temperature in the ranges 35–300 K and 5–150 K, respectively, in order to determine the Verwey temperature and the transition order. The AC susceptibility measurements were performed using a commercial CryoBIND system. Resistivity and AC magnetic susceptibility data are displayed in Fig. S1 and S2, respectively. Resistivity data show that the sample undergoes a first order metal-to-insulator transition (MIT) at a critical temperature of 116 K, lower than the typical values for highly-stoichiometric magnetite, as a result of the inherent impurity content of natural magnetite. As illustrated in Fig. S2, the AC magnetic susceptibility of our sample exhibits the same features reported in Refs. [24, 25] for synthetic stoichiometric crystals. In particular, in accordance to the latter studies, while in the critical temperature range there is no frequency dependence in the magnetic response, a strong frequency dependence characterizes the low-temperature susceptibility anomaly. The magnetization dynamics is interpreted according to Ref. [25], which ascribes it to domain wall motion (DWM). Accordingly, the drop in the real part of the AC magnetic susceptibility χ' results from crystal twinning across the structural transition, since the monoclinic ferroelastic domains created coincide with the magnetic domains and require higher applied fields to propagate via DWM compared to the cubic phase. Therefore, the temperature at which a first order discontinuity in χ' occurs is understood as the critical temperature for the structural transition and found to correspond to that for the MIT. A thermal hysteresis of about 0.3 K is also found within the transition temperature region between measurements on heating and cooling.

S2. OPTICAL CONDUCTIVITY

Fig. S3 displays the low-energy optical conductivity of magnetite. As the Verwey temperature is crossed, an optical gap opens below 140 meV, signaling the onset of the insulating phase. A spectral weight redistribution all the way to 2.5 eV accompanies the Verwey transition, evidence for the strongly correlated nature of magnetite [26]. Three main features are present in both the low- and high-temperature phase at 0.6, 2 and 5 eV. Based on LSDA calculations [27], Park et al. interpreted them as Fe^{2+} to Fe^{3+} B-site transitions, the optical absorption from the Fe^{3+} A- to the Fe^{2+} B-site and the charge transfer between the O $2p$ and the Fe $3d$ states, respectively [11]. Leonov et al. revised the latter assignment according to LDA+U calculations, proposing that the absorption features at 0.6 and 2 eV do not involve A-type Fe sites, but only B-type Fe sites with different valence states [28]. Although the overall agreement to the experimental data was improved compared to previous reports, the theoretical predictions failed to reproduce the correct energy and intensity of the 0.6 and 2 eV absorption features. A possible reason for the discrepancy is the assumption of the approximated P2/c unit cell along with the related class-I charge ordering pattern. Therefore, the assignment in Ref. [28] is still open to discussion.

S3. SPONTANEOUS RAMAN SCATTERING

Fig. S5 shows the spontaneous Raman spectra as a function of temperature. In the high-temperature phase they exhibit four main modes, designated according to Refs. [12, 13] as one A_{1g} and three t_{2g} modes. Their energies are in agreement with Ref. [12]. Some weak hematite impurities typical of natural magnetite crystals result in features marked by green arrows [29]. Degeneracy lifting across the Verwey transition gives rise to a fine structure of submodes, particularly between 250 and 400 cm^{-1} . Sharp features not related to any high-temperature mode also appear and are marked by red arrows. Based on the analysis presented in the main text, the two peaks at 124 and 163 cm^{-1} at 5 K are assigned to the X_4 and X_3 modes respectively. The temperature dependence of the higher energy modes has already been reported in literature [12, 13], and is in agreement with our results (see Fig. S6a–c). In contrast, the temperature dependence of the X_3 and X_4 modes associated to the metal-insulator transition is displayed in Fig. S6d–e for the first time.

S4. FLUCTUATION ASSISTED IMPULSIVE STIMULATED RAMAN SCATTERING

The activity of the coherent oscillations above the Verwey temperature T_V can be understood as a two-mode Raman process [30] involving a charge fluctuation with the charge density wave (CDW) ordering wave vector and a phonon with opposite momentum. We analyze the coupling with the Δ_5 or with the X_3 mode one at the time, but the analysis can be easily generalized to consider the two modes simultaneously.

We consider the following Hamiltonian which describes two generic normal modes of the system in the high-temperature phase (the modes will be specified below),

$$H_0 = \frac{1}{2} \sum_{\mathbf{q}\lambda=1,2} [P_{\mathbf{q}\lambda}P_{-\mathbf{q}\lambda} + \omega_{\mathbf{q}\lambda}^2 Q_{\mathbf{q}\lambda}Q_{-\mathbf{q}\lambda}] \quad (1)$$

Here $Q_{\mathbf{q}\lambda}$, $P_{\mathbf{q}\lambda}$ and $\omega_{\mathbf{q}\lambda}$ are the canonical coordinate, the conjugate momentum and the eigenfrequency for the normal mode with momentum \mathbf{q} belonging to branch λ .

The two-mode Raman Hamiltonian reads,

$$H_R = \sum_{\mathbf{q}} \delta K_{\mathbf{q}12}(t) Q_{\mathbf{q}1} Q_{-\mathbf{q}2} \quad (2)$$

with

$$\delta K_{\mathbf{q}12} = -\frac{V}{4} \boldsymbol{\mathcal{E}}(t) \frac{\partial^2 \chi}{\partial Q_{\mathbf{q}1} \partial Q_{-\mathbf{q}2}} (\omega_L) \boldsymbol{\mathcal{E}}^*(t) \quad (3)$$

Here we expressed the Raman tensor as a second derivative of the dielectric susceptibility [30, 31]. V is the sample volume and the pump electric field is modeled as $\mathbf{E}(t) = \boldsymbol{\mathcal{E}}(t)e^{i\omega_L t}$, with ω_L the central laser frequency and $\boldsymbol{\mathcal{E}}(t)$ describing the pump shape. Eq. (3) is averaged over one cycle of the pump central frequency.

H_R acts as a time-dependent interaction among the two modes which can be controlled by the laser field. The response of the modes can be computed via the Kubo formula. The linear response in $\delta K_{\mathbf{q}12}$ reads,

$$\langle Q_{\mathbf{q}1} Q_{-\mathbf{q}2} \rangle(t) = \int_{-\infty}^t dt' R(t-t') \delta K_{\mathbf{q}12}(t') \quad (4)$$

where

$$R(t) = -\frac{\hbar e^{-t/\tau}}{2\omega_{\mathbf{q}1}\omega_{\mathbf{q}2}} \times \left\{ \frac{1}{2} \left[\frac{1}{\tanh(\beta\hbar\omega_{\mathbf{q}1}/2)} + \frac{1}{\tanh(\beta\hbar\omega_{\mathbf{q}2}/2)} \right] \sin[(\omega_{\mathbf{q}1} + \omega_{\mathbf{q}2})t] - [n(\omega_{\mathbf{q}1}) - n(\omega_{\mathbf{q}2})] \sin[(\omega_{\mathbf{q}1} - \omega_{\mathbf{q}2})t] \right\} \quad (5)$$

with $\beta = 1/k_B T$, $n(\omega) = 1/(e^{\beta\hbar\omega} - 1)$ the Bose distribution function and τ a phenomenological relaxation time.

In principle the above Hamiltonian describes both spontaneous and Impulsive Stimulated Raman Scattering (ISRS), although, as discussed in the main text, only ISRS processes have been observed. In ISRS [31] the pump pulse determines the time dependence of $\delta K_{\mathbf{q}12}(t)$. At zero temperature, an impulsive form of $\delta K_{\mathbf{q}12}(t)$ produces a sine-like oscillation at the sum frequency of the two modes, while at finite temperatures both oscillations at the sum and difference frequency can be induced. Here, from the onset we assume that the two-mode process is Raman active, so the Raman tensor appearing in Eq. (3) is non-zero. The same matrix element evaluated at the frequency of the probe implies that the oscillations will show up as a time-dependent modulation of the differential reflectivity which can be detected in our setup [22, 23, 31, 32].

To model the oscillations observed above T_V we assume that $Q_{\mathbf{q}1}$ is one of the phonons which condense below T_V and $Q_{\mathbf{q}2}$ is the CDW order parameter of the Verwey transition. Thus, the excitation energies introduced in the main text are $E_{\text{phonon}} = \hbar\omega_{\mathbf{q}1}$ and $E_{\text{CDW}} = \hbar\omega_{\mathbf{q}2}$, with $\mathbf{q} \sim (0, 0, 1/2)$ for the Δ_5 mode and $\mathbf{q} \sim (0, 0, 1)$ for the X_3 mode (in units of $2\pi/a$, where a is the lattice parameter of the cubic structure). Close to T_V we expect $E_{\text{CDW}} \ll k_B T$, consistent with the quasielastic scattering observed with neutrons [21]. This should lead to peaks at $E_{\text{phonon}} \pm E_{\text{CDW}}$ in the Fourier transform of the traces, which may contribute to the broadening seen at $T = 200$ K in Fig. 3a of the main article. We attribute the peak at $T = 300$ K in the same panel (marked by a triangle) to the $E_{\text{phonon}} + E_{\text{CDW}}$ oscillation. The peak at $E_{\text{phonon}} - E_{\text{CDW}}$ expected in the low energy region is not resolved due to poorer sensitivity in this range.

To model the softening of the CDW mode, we assume a Landau potential of the form $\omega_{\mathbf{q}2}^2 = \alpha(T - T_V)$, with α a constant. In this limit, the response becomes,

$$R(t) = -\frac{\hbar k_B T e^{-t/\tau}}{2\omega_{\mathbf{q}1}\alpha(T - T_V)} \sin(\omega_{\mathbf{q}1}t) \quad (6)$$

which explains the oscillations seen at $T > T_V$ at a frequency close to the frequency of the phonon, which condenses for $T < T_V$.

In the presence of absorption at the pump frequency, $\delta K_{\mathbf{q}12}(t)$ may acquire a step form and the mechanism becomes displacive, yielding a cosine-like oscillation [20]. Below T_V , the CDW order parameter $\langle Q_{\mathbf{q}2} \rangle \neq 0$ at the ordering wave-vector, and Eq. (2) becomes a

one-phonon Raman Hamiltonian at this wave-vector, which explains ISRS and spontaneous Raman activity of the CDW related modes in the ordered phase.

The linear response is expected to break down for T greater than, but close to, T_V for sufficiently high fluence. To see this, we define the real coordinate $Q_\lambda = (Q_{\mathbf{q}\lambda} + Q_{-\mathbf{q}\lambda})/\sqrt{2}$ at the ordering wave-vector and express the potential energy as,

$$V(Q_1, Q_2) = \frac{1}{2}[\omega_1^2 Q_1^2 + \alpha(T - T_V)Q_2^2] + \delta K(t)Q_1 Q_2 \quad (7)$$

where we used the Landau form for the potential energy of the CDW order parameter. Stability of the disordered phase requires $V(Q_1, Q_2) > 0$, which implies $\delta K^2 < \omega_1^2 \alpha(T - T_V)$. Since δK^2 is proportional to the fluence, at sufficiently high fluence a transient instability is developed, which is expected to produce a non-linear response in the fluence, as indeed observed.

S5. SUPPLEMENTARY FIGURES

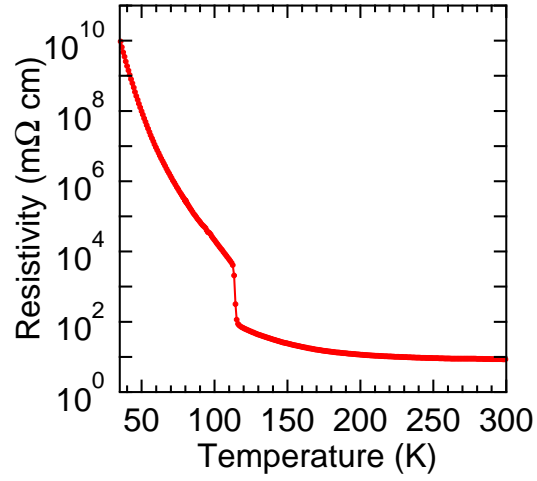


FIG. S1. Temperature dependence of the resistivity of our sample.

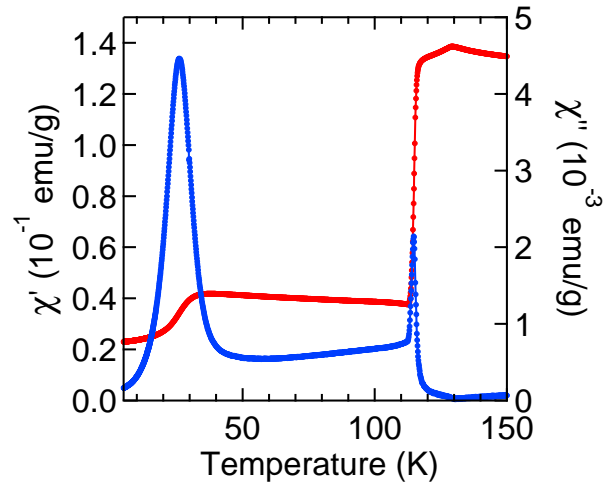


FIG. S2. Temperature dependence of the AC susceptibility of our sample (red line – real part χ' , blue line – imaginary part χ''). The frequency and amplitude of the driving field are 7 Hz and 0.64 Oe, respectively.

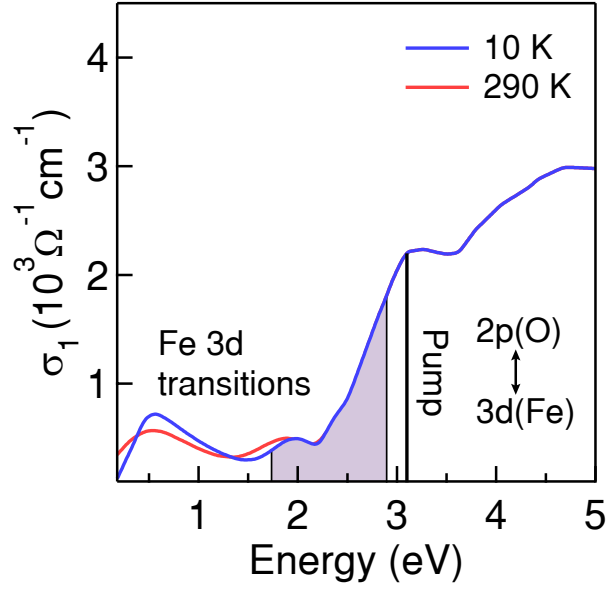


FIG. S3. Steady-state optical conductivity of magnetite at 10 and 290 K, adapted from [11]. A vertical black line indicates the pump photon energy. The shaded area corresponds to the spectral range of the broadband probe pulses.

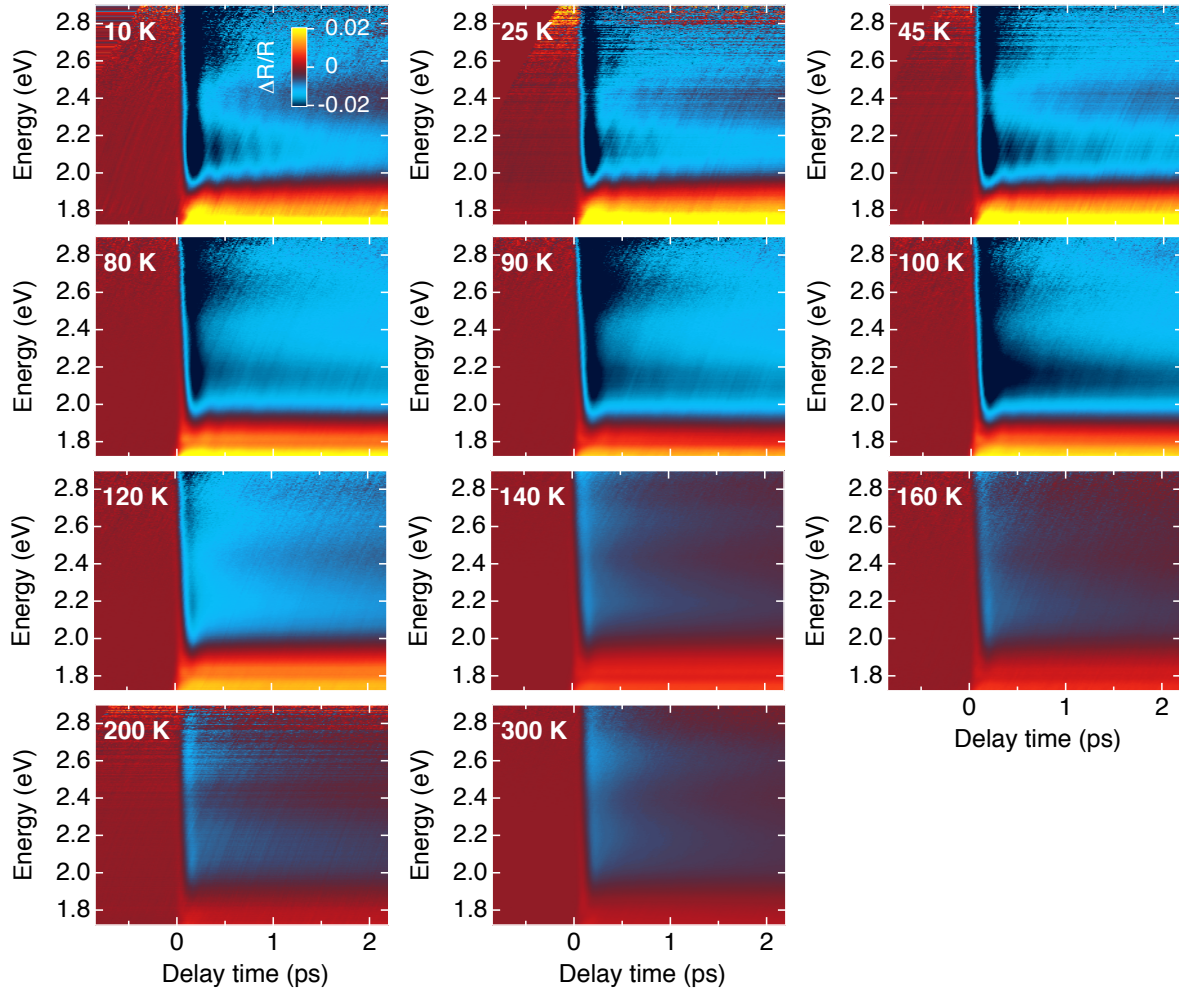


FIG. S4. Transient reflectivity spectra as a function of pump-probe time-delay at different temperatures above and below the Verwey temperature and an absorbed pump fluence of 3 mJ/cm^2 .

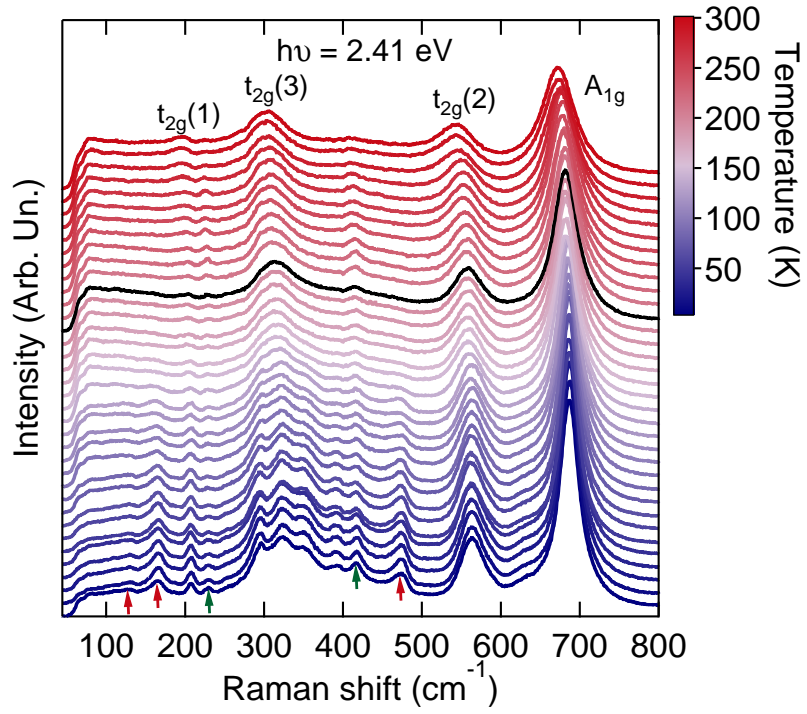


FIG. S5. Spontaneous Raman spectra of magnetite as a function of temperature. In the color scale, black corresponds to the Verwey temperature. Red and green arrows indicate the modes of the low-temperature structure and the peaks originating from the hematite impurities, respectively.

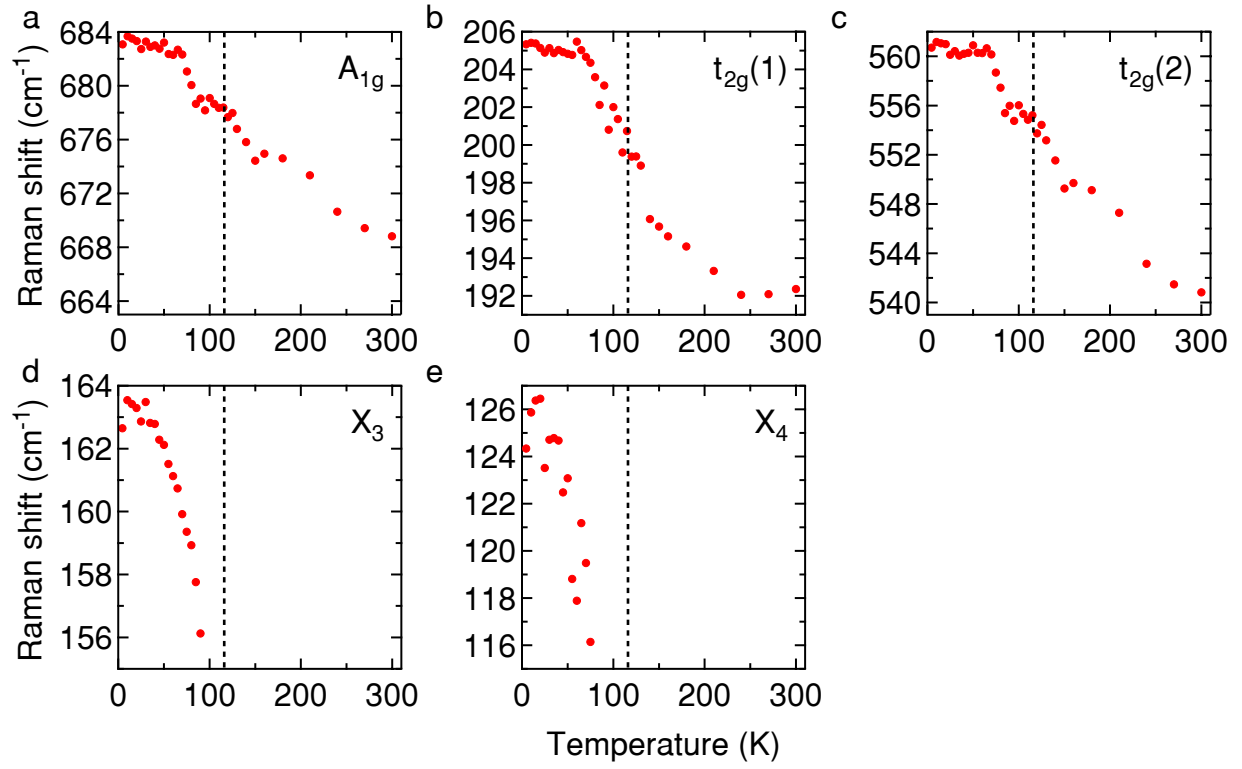


FIG. S6. Temperature dependence of the Raman shift of the main modes common to both the low- and high-temperature phase (a–c) and of the modes of the low-temperature structure (d–e). The dashed vertical line marks the Verwey temperature.